Chemistry–A European Journal
Research Article
doi.org/10.1002/chem.202304296
Chemistry Europe
European Chemical Societies Publishing
www.chemeurj.org

Constructing Hollow Microcubes SnS_2 as Negative Electrode for Sodium-ion and Potassium-ion Batteries

Chengping Li,*[a, b, c] Hongrui Yu,[a] Peng Dong,[c] Ding Wang,[c] Xiaoyuan Zeng,[c] Jinsong Wang,[a] Zhengfu Zhang,[a] Yingjie Zhang,[c] Angelina Sarapulova,[b, d, e] Xianlin Luo,[b] Kristina Pfeifer,[b] Helmut Ehrenberg,[b] and Sonia Dsoke*[b, d, e, f]

Sodium/potassium-ion batteries (NIBs and KIBs) are considered the most promising candidates for lithium-ion batteries in energy storage fields. Tin sulfide (SnS_2) is regarded as an attractive negative candidate for NIBs and KIBs thanks to its superior power density, high-rate performance and natural richness. Nevertheless, the slow dynamics, the enormous volume change and the decomposition of polysulfide intermediates limit its practical application. Herein, microcubes SnS_2 were prepared through sacrificial $MnCO_3$ template-assisted and a facile solvothermal reaction strategy and their performance was investigated in Na and K-based cells. The unique hollow cubic structure and well-confined SnS_2 nanosheets play an important role in Na^+/K^+ rapid kinetic and alleviating volume change. The effect of the carbon additives (Super P/C65) on the electrochemical properties were investigated thoroughly. The *in operando* and *ex-situ* characterization provide a piece of direct evidence to clarify the storage mechanism of such conversion-alloying type negative electrode materials.

Introduction

The need for high-capacity retention has prompted extensive investigation into developing multiple forms of sustainable power transformation and storage systems. Recently, LIBs have been employed in electric vehicles since the 1990s. However, the limited availability of lithium resources can't meet the growing demands of energy storage devices.[1–5] These motivations are triggering the investigation of NIBs and KIBs because of the natural richness of sodium and potassium resources. In addition, the potential of K^+/K (−2.92 V *vs.* [SHE]) is close to that of Li^+/Li (−3.04 V *vs.* [SHE]) and lower than that of Na^+/Na (−2.71 V *vs.* [SHE]), making NIBs and KIBs a good alternative to replace LIBs. Moreover, due to its affordable manufacturing process and impressive gravimetric energy density, aluminum foil serves as an excellent current collector for NIBs and KIBs. Recently, the development of negative electrode material for NIBs and KIBs has been a major effort.[6–11] However, NIB and KIB electrode materials are hindered by low specific capacity, unstable cycling performance, and sluggish charge transfer kinetics because Na^+ (1.06 Å) and K^+ (1.38 Å) have larger radius. Therefore, designing the negative electrode material capable of high reversible capacities and stable cyclical behavior is of great significance for NIBs and KIBs.

Up to now, many research works reported that some negative carbonaceous materials (soft carbon, graphite, and hard carbon) were explored for NIBs and KIBs.[12,13] Nevertheless, the Na and K storage performance of the commercial graphite is unsatisfactory. Many non-carbonaceous negative electrode materials, which can store the alkali ions via conversion and alloying mechanisms, have been investigated for NIBs and KIBs, showing enhanced specific capacity as opposed to carbon-containing.[14] Among the available choices, Sn-based metal sulfides stand out as promising candidates for negative electrodes, thanks to their high theoretical capacity.[15] Unfortunately, the main drawbacks of these negative electrode materials are the tremendous volume expansion and fast capacity decay upon cycling. Additionally, the larger radius compared to Li^+ results in slower Na^+ and K^+ diffusion and charge transfer kinetics. Therefore, some effective solutions to overcome the abovementioned questions were applied, in particular structural /morphological design and hybrid structure of the negative electrode materials. Recently, various morphologies with nanostructures (nanowalls, nanosheets, nanoparticles) have been investigated. Zhou *et al.*[16] developed a distinctive nanowall

[a] C. Li, H. Yu, J. Wang, Z. Zhang
Faculty of Materials Science and Engineering, Kunming University of Science and Technology, Kunming 650093, P. R. China
E-mail: li.cp@kust.edu.cn
[b] C. Li, A. Sarapulova, X. Luo, K. Pfeifer, H. Ehrenberg, S. Dsoke
Institute for Applied Materials (IAM), Karlsruhe Institute of Technology (KIT), Hermann-von-Helmholtz-Platz 1, Eggenstein-Leopoldshafen, 76344, Germany
[c] C. Li, P. Dong, D. Wang, X. Zeng, Y. Zhang
Faculty of Metallurgical and Energy Engineering, Kunming University of Science and Technology, Kunming 650093, P. R. China
[d] A. Sarapulova, S. Dsoke
Fraunhofer Institute for Solar Energy Systems, Dep. Electrical Energy Storage, Heidenhofstr.2, 79110 Freiburg, Germany
[e] A. Sarapulova, S. Dsoke
Freiburg Materials Research Center (FMF), Stefan-Meier-Straße 21, 79104 Freiburg, Germany
[f] S. Dsoke
Institute for Sustainable Systems Engineering (INATECH), University of Freiburg, Emmy-Noether-Straße 2, 79110 Freiburg, Germany
E-mail: sonia.dsoke@ise.fraunhofer.de

Supporting information for this article is available on the WWW under https://doi.org/10.1002/chem.202304296

electrode material, exhibiting a sodium storage performance of 576 mAh g^{-1}. Fang *et al.*[13] synthesized few-layered SnS_2-rGO nanosheets, providing a capacity of 448 mAh g^{-1} for KIBs. Designing nanostructured active material is beneficial for shortening diffusion paths for Na^+/K^+, enhancing electron transfer, increasing electrochemical reaction efficiency, and buffering the mechanical strain of repeated charge and discharge operations. However, the rational design and facile fabricated SnS_2-based architectures capable of highly exposed active sides, large surface area and excellent stability remain a significant challenge.

Using templates as precursors provides specific advantages compared to traditional synthesis routes, including the formation of different morphologies and porosities.[17] Hollow porous nanostructures can be fabricated through $MnCO_3$ as a sacrificial template. $MnCO_3$ has obtained much attention because of its different morphologies, large surface and void volume. Herein, we report microcubic SnS_2 consisting of ultra-thin nano-layers, which are grown with a microcubic $MnCO_3$ template. The detailed synthesis of homogeneous $MnCO_3$ microcubes in Supporting information. Microcubic $MnCO_3$ templates are removed through HCl solution washing, and hierarchical structured SnS_2 microboxes are finally obtained. The microcubes SnS_2 have highly exposed active sides, large surface area and excellent stability, therefore high performance of Na and K storage capacity are expected. Due to the inherently low conductivity of SnS_2, carbon agents (Super P/C65) are crucial for the percolation and electrochemical performance of SnS_2 material. However, studying the properties and the effect of different carbon additives in SnS_2-based electrodes is still lacking so far, the effect of the conductive agent (Super P/C65) on the electrochemical properties were investigated thoroughly. Microcubic SnS_2 is employed as the negative material in both Na and K half-cells to investigate its storage performance for sodium and potassium. Structural changes and morphologies various are investigated by *in operando* XRD and *ex*-situ SEM.

Results and Discussion

SnS_2 Microcubes Structural Characteristics and Surface Properties

Figure 1a shows XRD diffraction patterns of microcubic SnS_2, which agrees with SnS_2 (PDF#23-0677) with the space group of

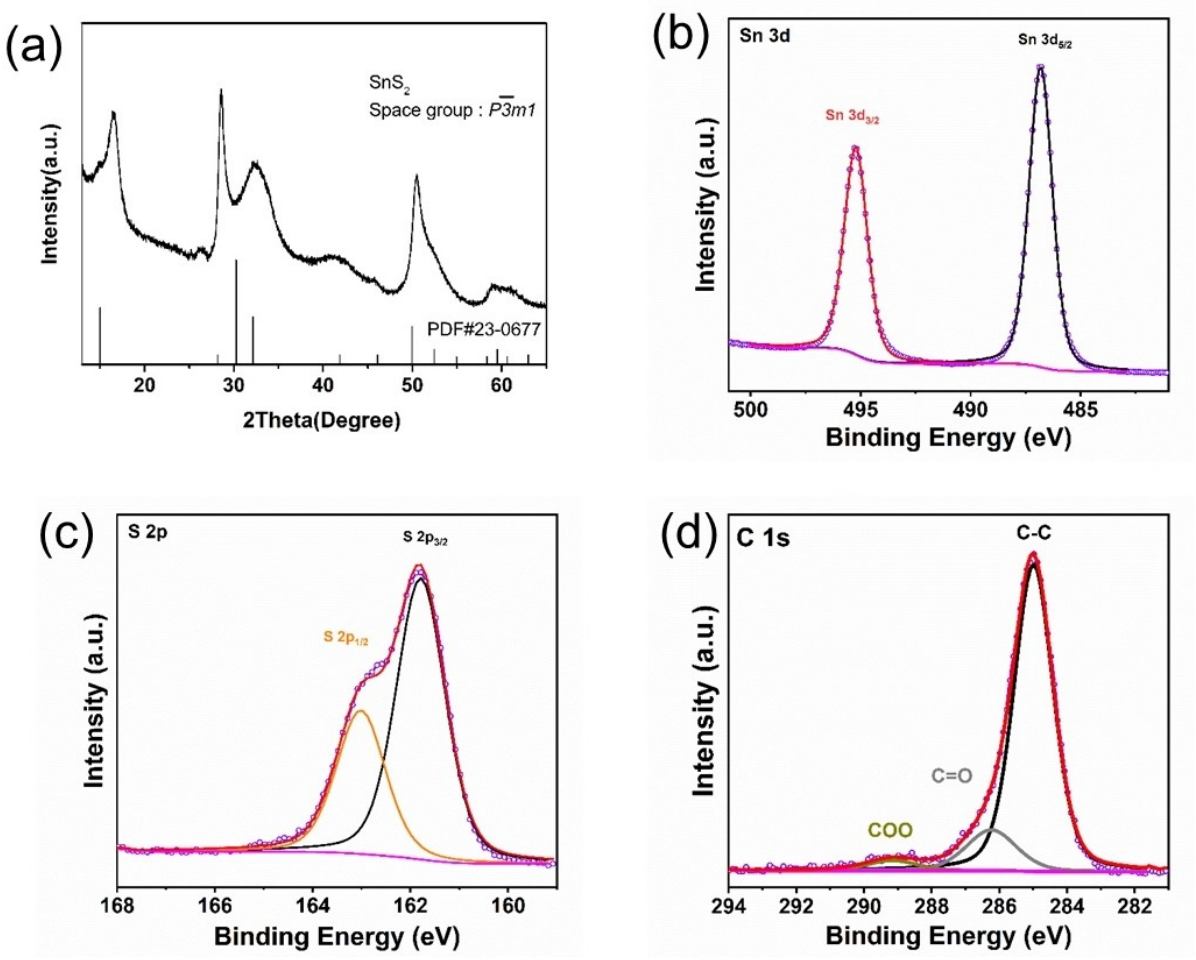

Figure 1. (a) XRD diffraction pattern and (b) Tin 3d, (c) sulfur 2p and (d) carbon 1s XPS spectra of the microcubic SnS_2 sample.

$P\bar{3}m1$. The $MnCO_3$ microcubes template are associated with trigonal $MnCO_3$ ($R\bar{3}c$, ICSD: 80868) in Figure S1.[18] The element states and chemical composition of as-prepared SnS2 was investigated by XPS measurements. As shown in Figure 1b, the Sn 3d spectrum, reveals two peaks at 495.3 (Sn $3d_{3/2}$) and 486.7 eV (Sn $3d_{5/2}$), confirming Sn (+4) in the SnS_2 sample.[12,19] In Figure 1c, peaks at 161.8 (S $2p_{3/2}$) and 163.1 eV (S $2p_{1/2}$) signify S (2−) in SnS_2. Moving to Figure 1d, the C 1s spectra exhibit three distinct peaks corresponding to 289.2 eV (O–C=O, 285.0 eV (C–C/C=C) and 286.2 eV (C–O), respectively.[20,21] These results confirmed that SnS_2 has been successfully synthesized.

$MnCO_3$ microcube templates are uniform with an average size of *ca.* 2–3 μm (Figure 2a). Owing to uniformity and microsize, $MnCO_3$ can work well as the template to support the subsequent growth of SnS_2 nanosheets. The SEM image of the $MnCO_3$@SnS_2 (Figure 2b) shows that $MnCO_3$ microcubes are uniformly coated with ultrathin SnS_2 nanosheets. After the $MnCO_3$ template was removed, the 3D hierarchical SnS_2 nanostructure was retained. We observe that a cracked SnS_2 microcube clearly shows a hollow interior (Figure 2c). The TEM image (Figure 2d) confirms the hollow cavity in the final sample, which agrees with the SEM results. Three diffraction rings with layer spacings of 0.61, 0.317, and 0.180 nm, correspond to the (001), (100), and (110) layers of SnS_2 in Figure 2f.[12,16,22] The SEM-EDS reveals the microcubic SnS_2 (Figure S2a) consisting of Tin (Figure S2b), S (Figure S2c), and C (Figure S2d), which indicates the homogeneous distribution of chemical composition in the SnS_2 nanosheets. Furthermore, the pronounced peak at 309.5 cm^{-1} is due to A_{1g} Raman-active vibrational mode. Additionally, Organic Elemental Analysis, detailed in Table S1, reveals a carbon content of 4.3 % (Figure S3).

Investigation of the Microcubes SnS_2 Electrode in Na-Half Cell

Our previous research demonstrated that fluoroethylene carbonate (FEC) additive enhanced cycling performance.[18] Therefore, subsequent electrochemical studies are performed with 5 wt % FEC.[23] The effect of carbon on an electrode is not univocal, but it depends on the electrode composition and can vary with the active material chosen (as well as with the microstructure properties of each active material). This study focuses on two different carbon additives (Super P and C65) on the Na^+-ion storage performance in the microcubic SnS_2 electrode. Figure 3a and b display the cyclic voltammetry (CV) plots for the SnS_2 electrode, respectively. At the first Na insertion process, the cathodic peak (1.72 V) presents the formation of Na_xSnS_2.[16,24] Then Na_xSnS_2 transfers to Na_2S and Sn with more Na^+ insertion, corresponding to one small peak at 1.07 V. With more Na^+-ion insertion into the microcubic SnS_2 electrode, the formed metallic Sn alloying with Na and the formation of Na–Sn alloying and the solid electrolyte interphase (SEI) occurs at 0.47 V.[22,25,26] Correspondingly, during the first desodiation process, $Na_{3.75}Sn$ de-alloyed and final conversed into Na_xSnS_2.[27] The SnS_2 + C65 electrode exhibits higher capacity retention than the SnS_2 + Super P electrode. The de-sodiation capacity increases during the first 10 cycles. Two reasons are possible for the de-sodiation capacity increase in the first 10 cycles. One is activation process: the SnS_2 electrode activation process continues for some cycles with a gradual capacity increase. The other one is pulverized SnS_2 nanoparticles are distributed on carbon additives after the first cycles, which can improve the electrochemical reaction efficiency between the SnS_2 nanoparticles and electrolyte. After that the de-sodiation capacity decreases upon cycling. Ex-situ SEM demonstrates the reason for the SnS_2 electrode specific capacity decrease from the 10th to 100rd cycle (Figure S4 and S5), The electrode consists of agglomerate nanoparticles and a large bulk after 10 cycles. The nanoparticle agglomeration transfers into a smaller one at the 100rd cycle, the formed smaller particle most probably is amorphous, which results in de-sodiation capacity decline upon cycling. Rate performances are conducted and shown in Figure 3d. The SnS_2 electrode, when combined with C65, exhibits enhanced rate performance and stability (Figure S6). Our previous research work demonstrated that Super P could cause active material to have more cracks and interrupt electronic conductive path, resulting in SnS_2 + Super P electrode having lower de-sodiation capacity.[18] The specific capacity experiences an initial increase for the first 20 cycles, followed by a decrease from 20 to 100 cycles (Figure S5). This could be due to the activation process and SEI formation.[28,29] The Na storage capacity of the microcubic SnS_2 electrode (with C65) reaches 208 mAh g^{-1} a notable improvement compared to the reported value of pure SnS_2 at 90 mAh g^{-1}.[30]

To further investigate the SnS_2 structural transformation when Na^+ insertion, the *in operando* XRD patterns during the 1st sodiation process were recorded. Some diffraction peaks of (001), (100), (101), (110) and (201) planes at 3.7°, 4.3°, 6.5°, 11.0° and 11.3°appear at the pristine stage (Figure 4a). During the sodiation process, the diffraction peaks (001) and (101) planes of the SnS_2 composite become weaker and shift to a lower 2θ angle. At the 1.06 V, It can be observed a serial of new diffraction peaks of Na_xSnS_2 (3.5°), Na_2S(4.2°, 6.0°), $Na_{15}S_4$ (7.0°) and Sn (9.6°) emerge, the Na_2S diffraction peak intensity gets stronger, implying the formation of Sn and sodium polysulfide, which corresponds well with the CV measurements. It is noteworthy that the small broad peak of $Na_{15}S_4$ is observed, indicating that the formed $Na_{15}S_4$ is amorphous.[31]

Ex-situ XPS were performed to get further understanding of the Na-ion storage mechanism. The fresh electrode shows the Sn 3d, S 2p and C 1s spectra (Figure S7a–c), which is consistent with the SnS_2 powder. At the sodiation of 0.01 V, the peaks of Sn $3d_{5/2}$ and Sn $3d_{3/2}$ disappear (Figure S7d), which is due to SEI layer formation and absorbs the corresponding photoelectrons. The broadening of the S 2p spectra in Figure S7e, indicates the conversion and alloying reactions, resulting in sodium polysulfides Na_2S_x ($2 < x < 8$) formation. The new C–C (283.7 eV) and CO_3 (290.0 eV) bonds imply the electrolyte decomposition (Figure S7f). At the de-sodiation of 3.0 V, the Sn 3d spectra appear and shift to lower binding energy compared with the fresh electrode, which corresponds to $Na_{3.75}Sn$ de-alloyed and finally conversed into Na_xSnS_2. The sharp S 2p spectra in Figure S7h, indicate the decomposition of sodium polysulfides. There is no obvious change in the C 1s (Figure S7i) compared

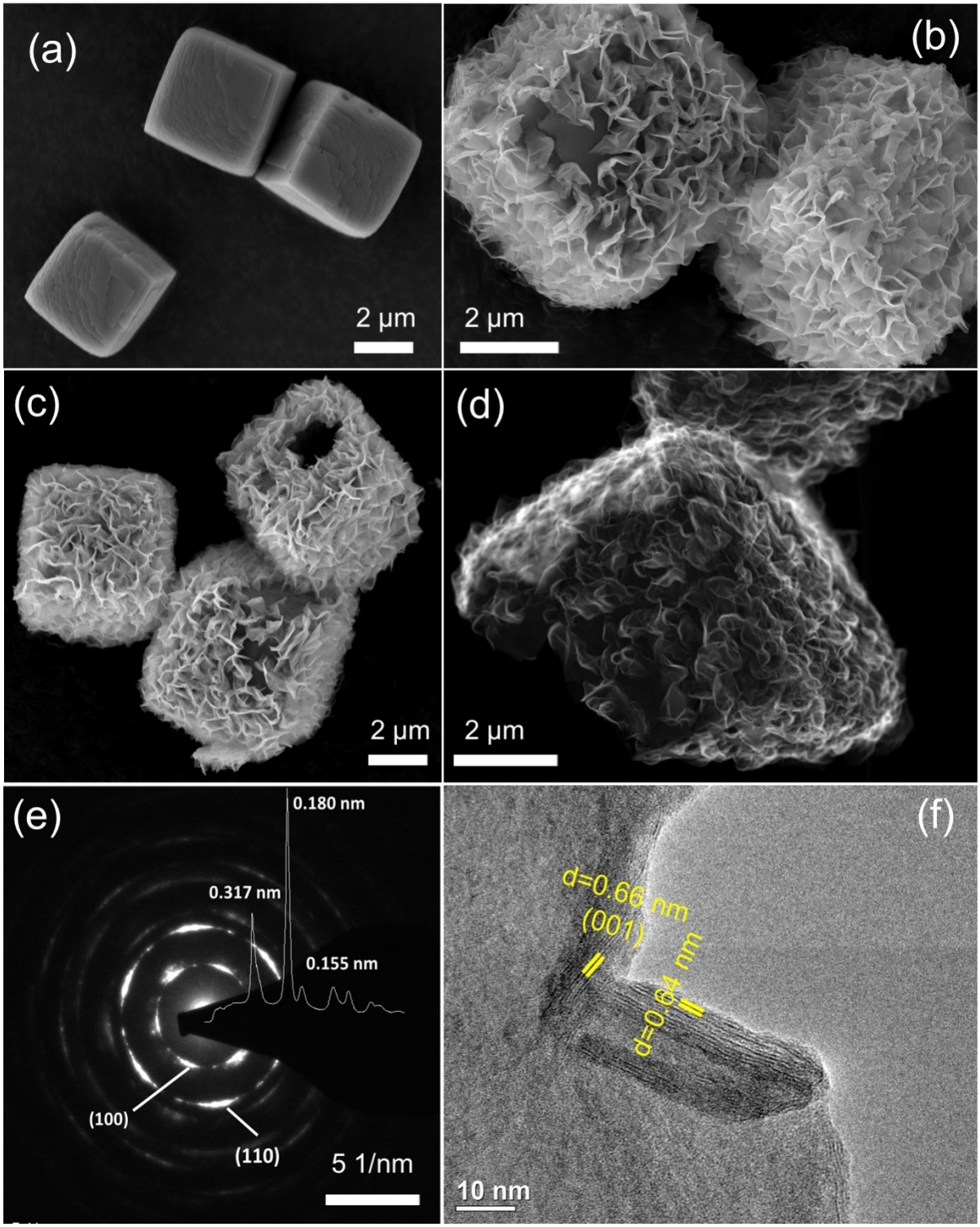

Figure 2. Surface morphologies of $MnCO_3$ (a), $MnCO_3$@SnS_2 (b), and microcubes SnS_2 nanosheets (c), TEM image of SnS_2 microcubes nanosheets (d), microcubes SnS_2 diffraction rings (e), SnS_2 microcubes nanosheets in HR-TEM (f).

with Figure S7f, which is due to the SEI layer continually forming.

Investigation of Kinetic Properties and Impedance Spectroscopy

Multi-scan CV tests were carried out to separate the surface- and diffusion-controlled reaction in the SnS_2 (Super P) and SnS_2

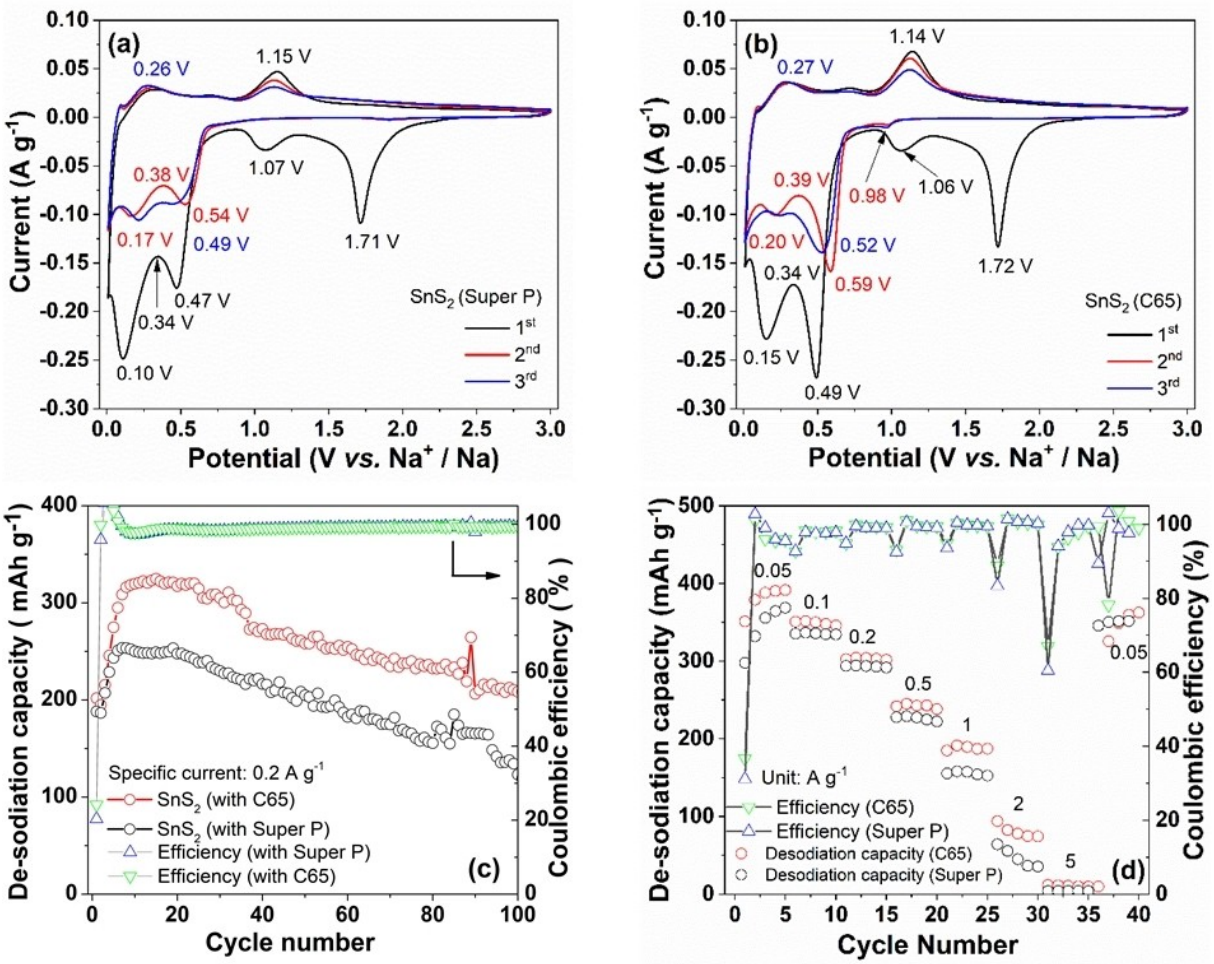

Figure 3. CV plots of the microcubic SnS_2 electrode (a–b); charge-discharge profiles and rate performance of the microcubic SnS_2 electrode at different specific currents (c–d).

(C65) electrode (Figure 5a and b). For both the SnS_2 (Super P) and SnS_2 (C65) electrodes, an increase in scan rates results in an escalation of the peak current. The peak current (i) and scanning speed (v) obey a power-law.[32–34] One anodic peak (1.20 V) was selected, by fitting the log (i) and log (v), the a and b values can be calculated.[35–37] The b value can be obtained for the SnS_2 + Super P ($b = 0.435$) and SnS_2 + C65 electrode ($b = 0.406$), respectively. This demonstrates diffusion behavior controls the electrochemical reaction during the initial cycles.

$$i = av^b \quad (1)$$

$$\log|(i)| = blog(v) + \log(a) \quad (2)$$

Electrochemical impedance spectroscopy (EIS) measurements were carried out to investigate the kinetics process in the Na half-cell. The Nyquist plots of the SnS_2 (Super P) electrode at 0.48 V from the 1st to 40th cycle as presented in Figure 6a and b. In parallel, Figure 6c and d illustrate the Nyquist plots at the same potential throughout the 1st to 40th cycles for the SnS_2 (C65) electrode. By building an equivalent circuit model to calculate the parameters, where R_{el} denotes the electrolyte resistance, encompassing components such as the separator and connectors in Figure 6e.[38–45] The R_{CT} semicircle diameter increases upon cycling in the SnS_2 + Super P electrode. This implies SEI layer becomes thicker with the cycle number increase. In the SnS_2 + C65 electrode, the diameter of the R_{CT} semicircle initially decreases and then stabilizes during the sodiation process. Conversely, there is an observable increase in the R_{CT} semicircle diameter in the de-sodiation process. This distinct trend in R_{CT} semicircle diameter variations could be due to different carbon additives, resulting in varied SEI thicknesses. The influence of the conductive carbon on the kinetics process is discussed later. Figure S8 presents R_{el}, R_{SEI}, and R_{CT} values for both the SnS_2 electrode with different carbon additives at various cycle states. The electrolyte resistance (R_{el}) remains stable for both electrodes. However, the higher R_{SEI} values for the SnS_2 (Super P) electrode compared to the SnS_2 (C65) electrode in the whole 40 cycles. This difference is likely associated with varying SEI layer thicknesses. The R_{CT} value increase in both electrode because Na^+ insertion results in electrode volume change and active particles lose contact.[46]

Ex-situ SEM is utilized to monitor alterations in surface morphology throughout the electrochemical process. Notably,

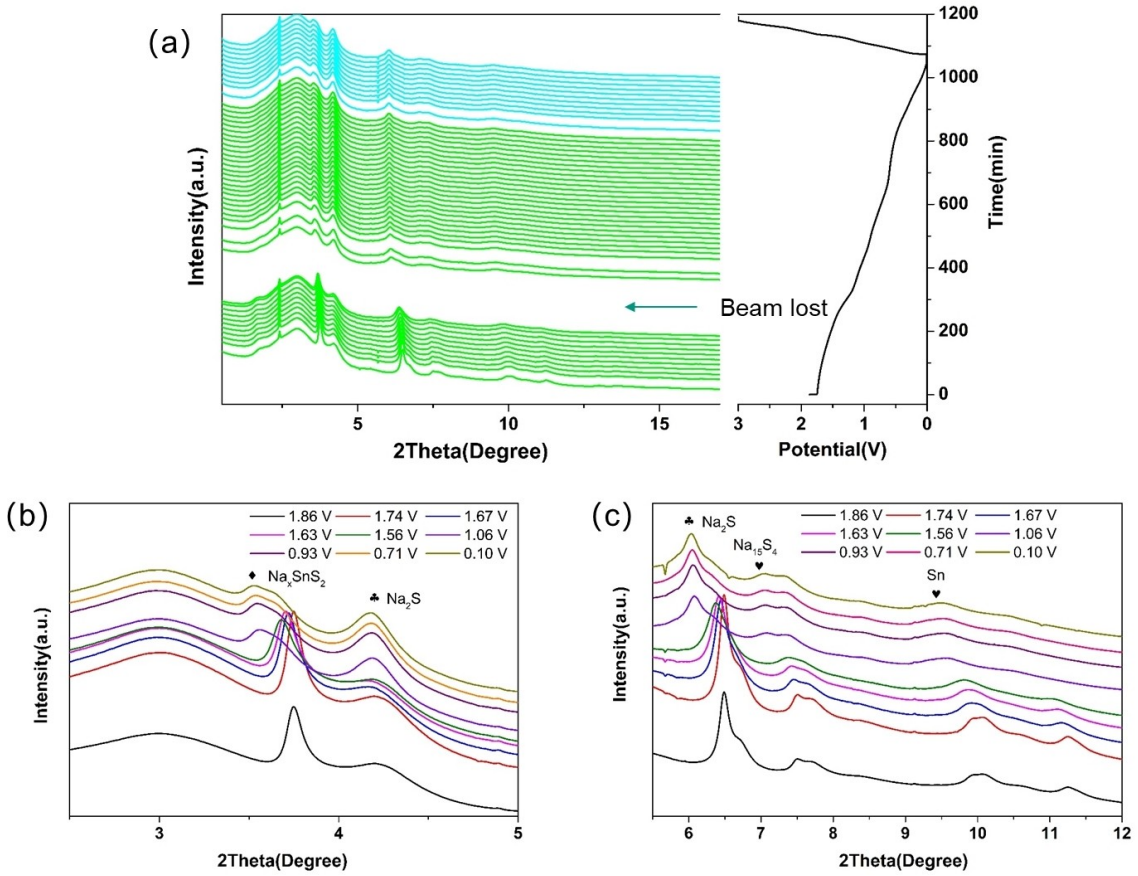

Figure 4. *In operando* XRD plots of the microcubic SnS_2 material and discharge-charge curves (a) during the 1st electrochemical measurement. The zoom areas of XRD in some chosen region (b) and (c).

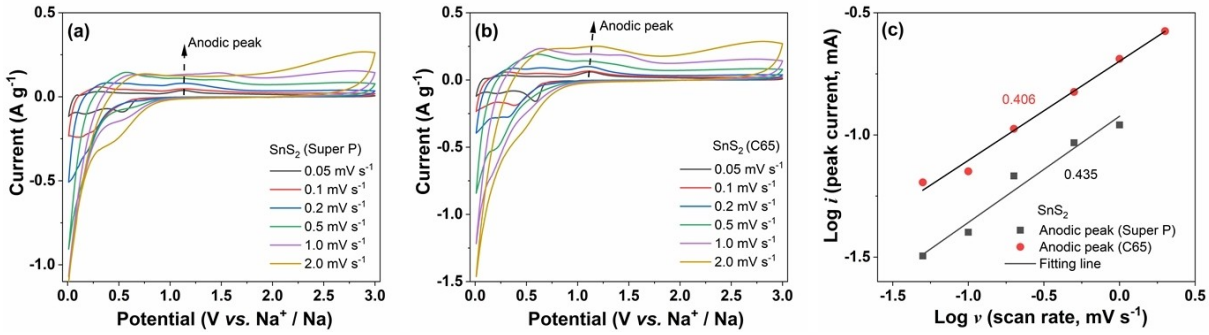

Figure 5. (a–b) Multi-scan CV plots of the microcubic SnS_2 electrode at different scanning speeds; *b*-value of the microcubic SnS_2 electrode by linear fitting at anodic peak 1.20 V (c).

nanoflakes interconnect with conductive carbon in the initial electrode, as illustrated in both Figure S9a and Figure S9d. The EDS elemental mapping (Figure S10a) indicates that microcubic SnS_2 and carbon additive material are homogenous. In the initial discharge process, the electrode's surface morphology (Figure S9b and e) exhibits a porous structure featuring numerous small spheres. The working electrode presents large aggregate and structure pulverization at the end of the 1st charge state (Figure S9c and f). The particles become smaller after the 1st de-sodiation process. EDS measurements confirm a uniform distribution of Tin, Sulfur, Na, and Carbon within sodiated products, along with an even distribution of Sn and S within desodiated products, as shown in Figure S10b and c. Based on the abovementioned analysis, it is demonstrated that Na^+-ion insertion into active material results in distinct cracks and large agglomeration in the sodiation state, while the crack of active material changed small when Na^+-ion extraction.

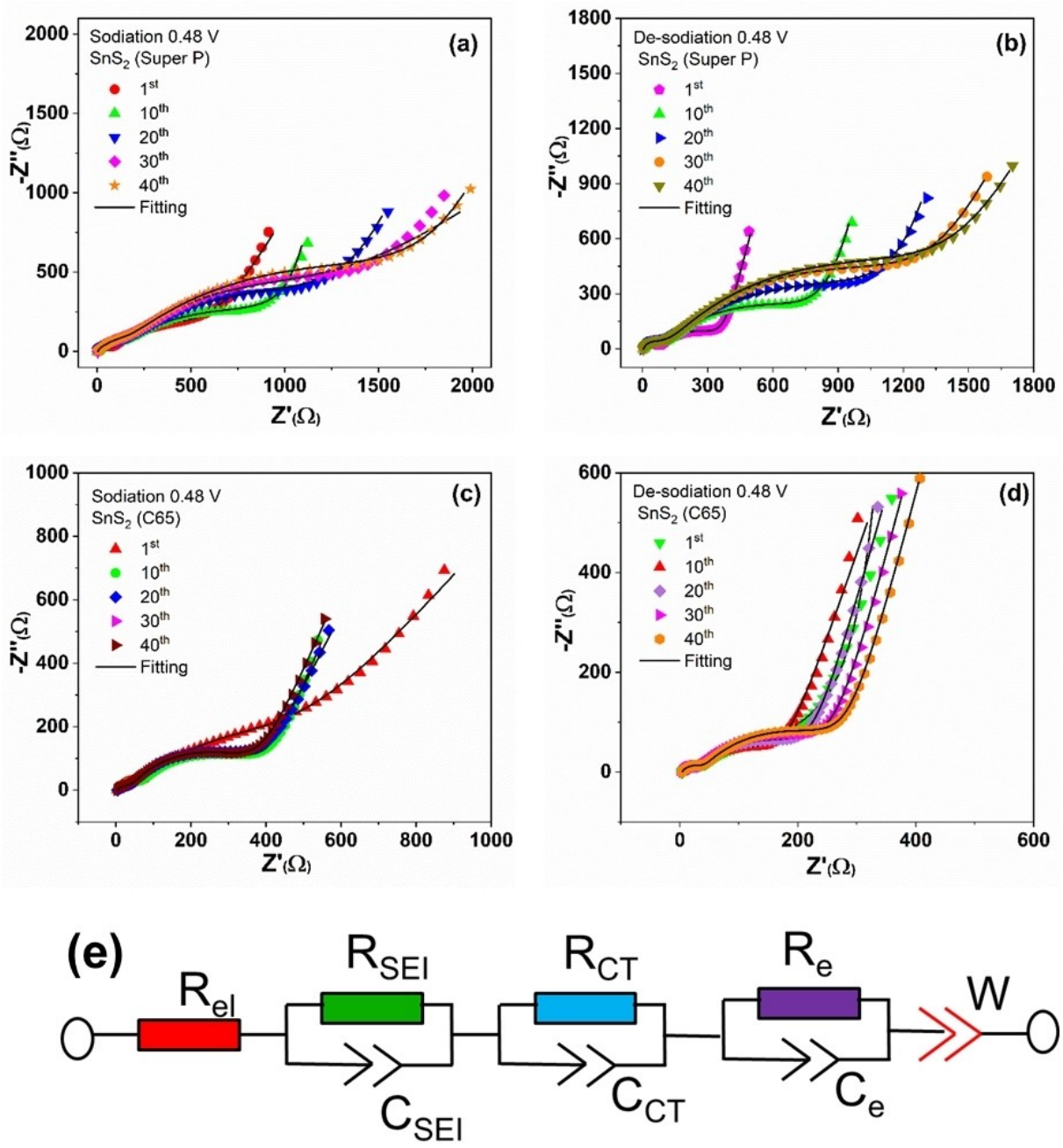

Figure 6. The Nyquist plots of the microcubic SnS_2 electrode with two different carbon additives at the potential of 0.48 V sodiated (a, c) and de-sodiated states (b, d); the equivalent circuit model (e).

Study on K Storage Performance and Kinetic Characterization

The SnS_2 electrode shows good electrochemical behaviors in NIBs. Hence, it's valuable to further explore the K storage performance. Cyclic voltammetry (CV) plots for the SnS_2 electrode during the initial cycles in KIBs are depicted in Figure 7a and b. In the initial K-ion insertion process, the SnS_2 phase transfers to the SnS and K_2S (1.92/1.94 V).[47–50] Additionally, the cathodic peaks (0.75, 0.5 V) are associated with Sn and SEI layer formation. Finally, the metallic Sn alloying with K (K_4Sn_{23} and KSn) appeared at 0.15 V. These abovementioned peaks become weaker at the 2nd to 5th cycle, this is because of some irreversible phase transition and amorphization processes. Similarly, the peak spanning from 0.52 V to 1.05 V corresponds to KSn de-alloying and the formation of K_xSnS_2 during the 1st de-potassiation process. The favorable electrochemical reversibility of SnS_2 in the potassiation and de-potassification reactions is evident through the substantial overlap of CV curves.

Ex-situ XPS analyses were carried out to study the K-ion storage behaviors of the microcubes SnS_2. Similarly, the high resolution of the Sn 3d, S 2p and C 1s spectra of the fresh electrode agrees well with the SnS_2 powder (Figure S12a–c).

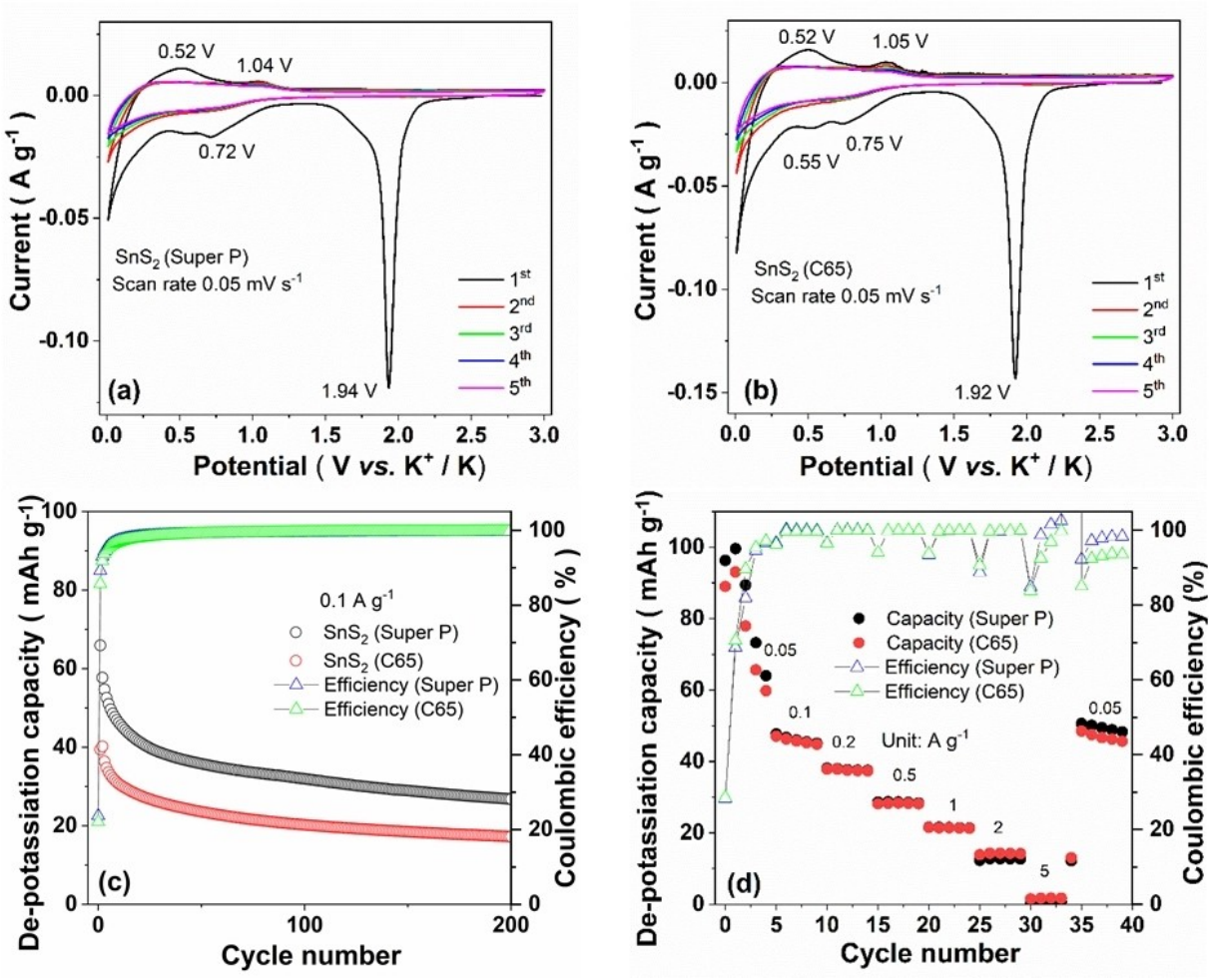

Figure 7. Cyclic voltammetry (CV) curves (a–b), charge-discharge profile and rate performance for both miscrocubic SnS_2 electrodes in a potassium-ion half-cell with different carbon additives, respectively (c–d).

The Sn 3d spectra disappear when potassiation to 0.01 V, and the broadening of S 2p are observed in Figure S12d–e, which is attributed to SnS_2 transfers to SnS, K_2S, metallic Sn and K–Sn alloying products. The new C–C (283.8 eV) and CO_3 (290.8 eV) bonds indicate the decomposition of EC, DMC and KFSI (Figure S12f). When de-potassiation to 3.0 V, the Sn 3d shows broadening of Sn $3d_{3/2}$, which is related to KSn de-alloying and the formation of K_xSnS_2 during the 1st de-potassiation process. The S 2p spectra becomes shrap and small broaden peak appears (160.0 eV), which is due to potassium polysulfides K_2S_x ($2 < x < 8$) decomposition (Figure S12g–h). The C 1s spectra shows sharp peak of C–C (284.2 eV) at the de-potassiation of 3.0 V, which is could be due to SEI decomposition during the charge process (Figure S12i).

The de-potassiation capacity diminishes with an increase in cycling numbers for both the SnS_2 (Super P) and SnS_2 (C65) electrodes (Figure 7c). The SnS_2 (Super P) and SnS_2 (C65) electrodes display the same tendency and stable capacity retention at all specific currents (Figure 7d). The SnS_2 (Super P) electrode yields a de-potassiation capacity (36 mAh g^{-1}, 0.1 A g^{-1}). This surpasses the reported pure SnS_2 electrode capacity (21 mAh g^{-1} for at the same current) (Figure S11). To delve deeper into the surface- and diffusion-controlled behavior for SnS_2 electrode in K half-cell, multiple-scan CV measurements were conducted (Figure 8). A prominent anodic peak was selected for investigation, and upon linear fitting the log (*i*) and log (*v*), both the SnS_2 (Super P) and SnS_2 (C65) electrodes exhibit *b* value of 0.89. This suggests that the potassiation and de-potassiation process is governed by the surface capacitive process.

Figure 9 shows the Nyquist plots of the microcubic SnS_2 electrode in the K half-cell. The semicircle diameter increases from the 1st to the 40th cycle, indicating a rise in R_{CT} with more K^+-ion insertion. The semicircle diameter of SnS_2 + Super P is consistently smaller than that of the SnS_2 + C65 electrode at each cycle, indicating a smaller R_{CT} value when using Super P additive. Additionally, the R_{SEI} values for both the SnS_2 (Super P) and SnS_2 (C65) electrodes were determined using the Relaxis 3 software, as illustrated in Figure S13. R_{SEI} values of the SnS_2 (C65) electrode increase from 5148 Ω (1st cycle) to 5793 Ω (40th cycle) during the K^+ insertion process, R_{SEI} values decrease from 6605 Ω (1st cycle) to 3028 Ω (40th cycle) during K^+ extraction

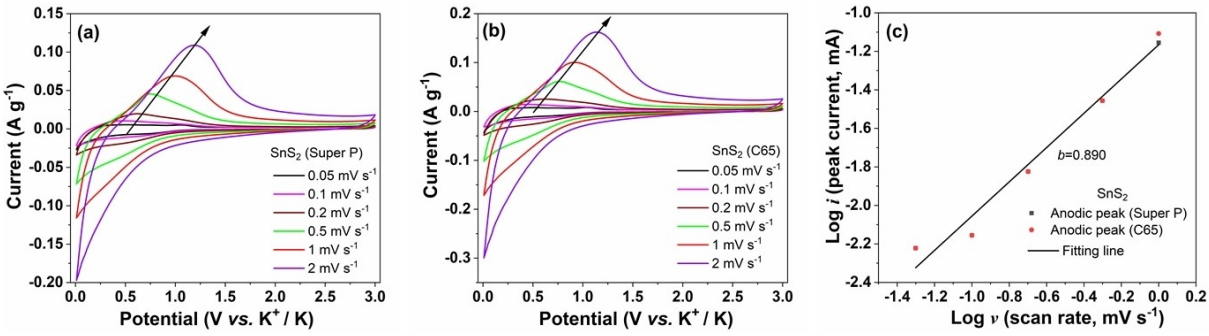

Figure 8. Multi-scan CV at various scanning speeds (a–b); the log *i* and log *v* at one selected peak(c).

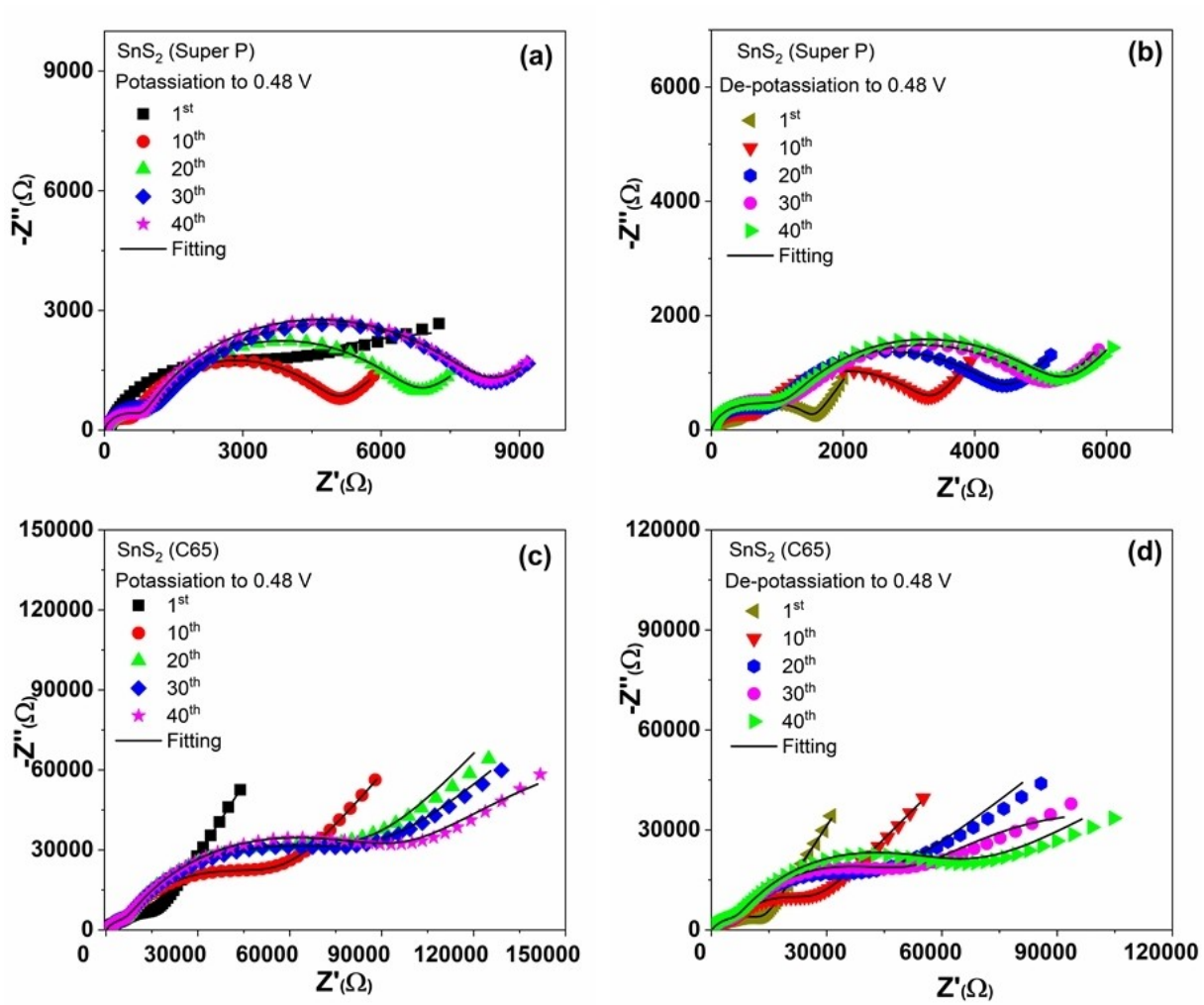

Figure 9. The Nyquist plots of the microcubic SnS_2 electrode at the potential of 0.48 V at the potassiated (a, c) and de-potassiated state (b, d);

process. While R_{SEI} values of the SnS_2 (Super P) electrode shows different changing tendency. R_{SEI} values decrease from 2755 Ω (1^{st} cycle) to 736 Ω (40^{th} cycle) during the K^+ insertion process and slightly increase from 362 Ω (1^{st} cycle) to 420 Ω (40^{th} cycle) during the K-ion extraction process. These different R_{SEI} value-changing tendencies could be related to SEI thickness and electrode surface homogeneity when changing conductive carbon. The surface morphologies of the SnS_2 (Super P) electrode reveals noticeable cracks and extensive aggregation after the first potassiation. There is some bigger bulk with 1–2 μm and some cavities in the following process (Figure S14). The elemental distribution analysis of the SnS_2 (Super P) electrode demonstrates a consistent dispersion of Tin, Sulfur, and potassium in both the discharged and charged electrodes (Figure S15).

Conclusions

SnS_2 microcubes were prepared through sacrificial $MnCO_3$ template-assisted and a facile solvothermal reaction strategy, and investigated their electrochemical performance in Na- and K-half cell. The unique hollow cubic structure and well-confined SnS_2 nanosheets improve Na^+/K^+ -ion insertion/extraction and alleviate volume expansion. At 0.2 $A\,g^{-1}$, the SnS_2 +C65 electrode achieves a de-sodiation capacity of 208 $mAh\,g^{-1}$. This performance surpasses the reported capacity of pure SnS_2, which is 90 $mAh\,g^{-1}$ (0.1 $A\,g^{-1}$). Due to the Super P have higher Na storage capacity leading to more volume expansion, therefore, the SnS_2 (C65) electrode shows enhanced Na storage capacity. In comparison, the function of the Super P and C65 is different in K storage performance. This could be owing to the K^+ storage mechanism being different from Na-ion.

Notes

The authors declare no competing financial interest.

Supplementary materials

The Supporting Information is available free of charge at https://chemistry-europe.onlinelibrary.wiley.com/doi/abs/10.1002/chem.202304296 SEM and TEM photographs of the micro-cubic SnS_2; the OEA analysis; The electrochemical behavior of the SnS_2 (Super P) and SnS_2 (C65) electrode in Na and K-half cell.

Author Contributions

Chengping Li: Supervision, Methodology, Investigation, Writing. **Hongrui Yu**: Data curation, Methodology, Formal analysis**. Peng Dong**: Investigation, Methodology. **Ding Wang**: Investigation, Methodology, review & editing. **Xiaoyuan Zeng**: Investigation, Methodology. **Jinsong Wang**: Investigation, Methodology. **Zhengfu Zhang**: Investigation, Methodology; **Yingjie Zhang**: Funding acquisition, investigation. **Angelina Sarapulova**: Discussion, Writing. **Xianlin Luo**: Investigation, Methodology. **Kristina Pfeifer**: Investigation, Methodology, review & editing. **Helmut Ehrenberg**: Supervision, Funding acquisition, revising the manuscript. **Sonia Dsoke**: Investigation, Discussion, Funding acquisition, revising manuscript.

Acknowledgements

C. Li is grateful to the China Scholarship Council (CSC, No.: 201707030004) for provision of the financial support. The authors are also grateful to DESY (Hamburg, Germany) for the provision of *in operando* measurements. We thank for the financial support of Yunnan Fundamental Research Projects (202201BE070001-019 and 202301AT070167) and Yunnan Major Scientific and Technological Projects (202202AG050003). The authors acknowledge the financial support from German Research Foundation (DFG) under Project ID 390874152 (POLiS Cluster of Excellence, EXC 2154). Open Access funding enabled and organized by Projekt DEAL.

Conflict of Interests

The authors declare no conflict of interest.

Data Availability Statement

The data that support the findings of this study are available in the supplementary material of this article.

Keywords: Microcubes SnS_2 · nanosheets · *in operando* XRD · Na/K storage

[1] K. Chayambuka, G. Mulder, D. L. Danilov, P. H. L. Notten, *Adv. Energy Mater.* **2018**, *8(16)*, 1800079.
[2] X. Wu, D. P. Leonard, X. Ji, *Chem. Mater.* **2017**, *29(12)*, 5031–5042.
[3] W. Zhang, Z. Wu, J. Zhang, G. Liu, N.-H. Yang, R.-S. Liu, W. K. Pang, W. Li, Z. Guo, *Nano Energy* **2018**, *53*, 967–974.
[4] L. Fan, R. Ma, Q. Zhang, X. Jia, B. Lu, *Angew. Chem. Int. Ed.* **2019**, *58(31)*, 10500–10505.
[5] P. K. Nayak, L. Yang, W. Brehm, P. Adelhelm, *Angew. Chem. Int. Ed.* **2018**, *57(1)*, 102–120.
[6] L. Liu, Y. Chen, Y. Xie, P. Tao, Z. Wang, Q. Li, K. Wang, C. Yan, *Small* **2019**, *15(5)*, 1804158.
[7] Y. L. Bai, Y. S. Liu, C. Ma, K. X. Wang, J. S. Chen, *ACS Nano* **2018**, *12(11)*, 11503–11510.
[8] Y. Liu, Z. Tai, J. Zhang, W. K. Pang, Q. Zhang, H. Feng, K. Konstantinov, Z. Guo, H. K. Liu, *Nat. Commun.* **2018**, *9(1)*, 3645.
[9] W. Zhang, J. Mao, S. Li, Z. Chen, Z. Guo, *J. Am. Chem. Soc.* **2017**, *139(9)*, 3316–3319.
[10] X. Pei, Y. Zhu, C. Du, H. Peng, Z. Wang, X. Ma, J. Hou, C. Cao, *ACS Appl. Energ. Mater.* **2023**, *6(15)*, 8132–8140.
[11] B. Liu, L. Wang, Y. Zhu, H. Peng, C. Du, X. Yang, Q. Zhao, J. Hou, C. Cao, *ACS Nano* **2022**, *16(8)*, 12900–12909.
[12] L. Fan, X. Li, X. Song, N. Hu, D. Xiong, A. Koo, X. Sun, *ACS Appl. Mater. Interfaces* **2018**, *10(3)*, 2637–2648.
[13] L. Fang, J. Xu, S. Sun, B. Lin, Q. Guo, D. Luo, H. Xia, *Small* **2019**, *15(10)*, 1804806.
[14] W. Wang, B. Jiang, C. Qian, F. Lv, J. Feng, J. Zhou, K. Wang, C. Yang, Y. Yang, S. Guo, *Adv. Mater.* **2018**, *30(30)*, 1801812.
[15] L. Wang, Q. Zhao, Z. Wang, Y. Wu, X. Ma, Y. Zhu, C. Cao, *Nanoscale* **2020**, *12(1)*, 248–255.
[16] P. Zhou, X. Wang, W. Guan, D. Zhang, L. Fang, Y. Jiang, *ACS Appl. Mater. Interfaces* **2017**, *9(8)*, 6979–6987.
[17] C. Du, W. Younas, Z. Wang, X. Yang, E. Meng, L. Wang, J. Huang, X. Ma, Y. Zhu, C. Cao, *J. Mater. Chem. A* **2021**, *9(6)*, 3648–3656.
[18] C. Li, K. Pfeifer, X. Luo, G. Melinte, J. Wang, Z. Zhang, Y. Zhang, P. Dong, A. Sarapulova, H. Ehrenberg, et al., *ChemSusChem* **2023**, *16(7)*, e202202281.
[19] Y. Zhang, P. Zhu, L. Huang, J. Xie, S. Zhang, G. Cao, X. Zhao, *Adv. Funct. Mater.* **2015**, *25(3)*, 481–489.
[20] Y. Jiang, Y. Feng, B. Xi, S. Kai, K. Mi, J. Feng, J. Zhang, S. Xiong, *J. Mater. Chem. A* **2016**, *4(27)*, 10719–10726.
[21] Z. Wang, Y. Dong, H. Li, Z. Zhao, H. Bin Wu, C. Hao, S. Liu, J. Qiu, X. W. Lou, *Nat. Commun.* **2014**, *5(1)*, 5002.
[22] J. Cui, S. Yao, Z. Lu, J. Huang, W. G. Chong, F. Ciucci, J. Kim, *Adv. Energy Mater.* **2018**, *8(10)*, 1702488.
[23] K. Pfeifer, S. Arnold, Ö. Budak, X. Luo, V. Presser, H. Ehrenberg, S. Dsoke, *J. Mater. Chem. A* **2020**, *8(12)*, 6092–6104.
[24] J. Wang, C. Luo, J. Mao, Y. Zhu, X. Fan, T. Gao, A. C. Mignerey, C. Wang, *ACS Appl. Mater. Interfaces* **2015**, *7(21)*, 11476–11481.

[25] B. Qu, C. Ma, G. Ji, C. Xu, J. Xu, Y. S. Meng, T. Wang, J. Y. Lee, *Adv. Mater.* **2014**, *26(23)*, 3854–3859.
[26] Y. Liu, H. Kang, L. Jiao, C. Chen, K. Cao, Y. Wang, H. Yuan, *Nanoscale* **2015**, *7(4)*, 1325–1332.
[27] W. Sun, X. Rui, D. Yang, Z. Sun, B. Li, W. Zhang, Y. Zong, S. Madhavi, S. Dou, Q. Yan, *ACS Nano* **2015**, *9(11)*, 11371–11381.
[28] Y. Ren, J. Wang, X. Huang, J. Ding, *Mater. Lett.* **2017**, *186*, 57–61.
[29] Z. Zhang, H. Zhao, J. Fang, X. Chang, Z. Li, L. Zhao, *ACS Appl. Mater. Interfaces* **2018**, *10(34)*, 28533–28540.
[30] L. Zeng, L. Zhang, X. Liu, C. Zhang, *Nanomaterials* **2020**, *10(12)*, 1–11.
[31] Q. Sun, D. Li, L. Dai, Z. Liang, L. Ci, *Small* **2020**, *16(45)*, 2005023.
[32] G. A. Muller, J. B. Cook, H.-S. Kim, S. H. Tolbert, B. Dunn, *Nano Lett.* **2015**, *15(3)*, 1911–1917.
[33] G. Tian, Z. Zhao, A. Sarapulova, C. Das, L. Zhu, S. Liu, A. Missiul, E. Welter, J. Maibach, S. Dsoke, *J. Mater. Chem. A* **2019**, *7(26)*, 15640–15653.
[34] V. Augustyn, J. Come, M. A. Lowe, J. W. Kim, P.-L. Taberna, S. H. Tolbert, H. D. Abruña, P. Simon, B. Dunn, *Nat. Mater.* **2013**, *12(6)*, 518–522.
[35] T. Brezesinski, J. Wang, S. H. Tolbert, B. Dunn, *Nat. Mater.* **2010**, *9(2)*, 146–151.
[36] L. Li, S. Peng, N. Bucher, H. Y. Chen, N. Shen, A. Nagasubramanian, E. Eldho, S. Hartung, S. Ramakrishna, M. Srinivasan, *Nano Energy* **2017**, *37*, 81–89.
[37] H. Lindström, S. Södergren, A. Solbrand, H. Rensmo, J. Hjelm, A. Hagfeldt, S. E. Lindquist, *J. Phys. Chem. B* **1997**, *101(39)*, 7717–7722.
[38] C. Li, A. Sarapulova, Z. Zhao, Q. Fu, V. Trouillet, A. Missiul, E. Welter, S. Dsoke, *Chem. Mater.* **2019**, *31(15)*, 5633–5645.
[39] F. Nobili, S. Dsoke, M. Mancini, R. Tossici, R. Marassi, *J. Power Sources* **2008**, *180(2)*, 845–851.
[40] J. Y. Xiang, X. L. Wang, X. H. Xia, J. Zhong, J. P. Tu, *J. Alloys Compd.* **2011**, *509(1)*, 157–160.
[41] G. Carbonari, F. Maroni, M. Pasqualini, R. Tossici, F. Nobili, *Electrochim. Acta* **2017**, *247*, 392–399.
[42] F. Maroni, S. Gabrielli, A. Palmieri, E. Marcantoni, F. Croce, F. Nobili, *J. Power Sources* **2016**, *332*, 79–87.
[43] J. Zhu, Y. Wang, Y. Huang, R. Bhushan Gopaluni, Y. Cao, M. Heere, M. J. Mühlbauer, L. Mereacre, H. Dai, X. Liu, et al., *Nat. Commun.* **2022**, *13(1)*, 2261.
[44] J.-M. Tarascon, M. Armand, *Nature* **2001**, *414(6861)*, 359–367.
[45] J. Huang, Z. Jiang, *Electrochim. Acta* **2008**, *53(26)*, 7756–7759.
[46] K. Pfeifer, S. Arnold, Ö. Budak, X. Luo, V. Presser, H. Ehrenberg, S. Dsoke, *J. Mater. Chem. A* **2020**, *8(12)*, 6092–6104.
[47] J. Xie, Y. Zhu, N. Zhuang, X. Li, X. Yuan, J. Li, G. Hong, W. Mai, *J. Mater. Chem. A* **2019**, *7(33)*, 19332–19341.
[48] L. Cao, B. Zhang, X. Ou, C. Wang, C. Peng, J. Zhang, *ChemElectroChem* **2019**, *6(8)*, 2254–2263.
[49] K. Huang, Z. Xing, L. Wang, X. Wu, W. Zhao, X. Qi, H. Wang, Z. Ju, *J. Mater. Chem. A* **2018**, *6(2)*, 434–442.
[50] C. Sheng, C. Zhang, X. Shen, S. Zhao, L. Fu, Y. Wu, J. Wang, Y. Chen, *Batteries & Supercaps* **2020**, *3(1)*, 56–59.

Manuscript received: December 22, 2023
Accepted manuscript online: February 21, 2024
Version of record online: March 18, 2024